Simulation of Synthetic Jets in Quiescent Air Using Unsteady Reynolds Averaged Navier-Stokes Equations

Veer N. Vatsa[*]

NASA Langley Research Center, Hampton, VA 23681

Eli Turkel[†]

Tel-Aviv University, Israel and NIA, Hampton, VA 23681

Abstract

We apply an unsteady Reynolds-averaged Navier-Stokes (URANS) solver for the simulation of a synthetic (zero net mass flow) jet created by a single diaphragm piezoelectric actuator in quiescent air. This configuration was designated as Case 1 for the CFDVAL2004 workshop held at Williamsburg, Virginia, in March 2004. Time-averaged and instantaneous data for this case were obtained at NASA Langley Research Center, using multiple measurement techniques. Computational results from two-dimensional simulations with one-equation Spalart-Allmaras and two-equation Menter's turbulence models are presented along with the experimental data. The effect of grid refinement, preconditioning, and time-step variation are also examined.

Introduction

Significant interest has been growing in the aerospace community in the field of flow control in recent years. An entire AIAA conference is now devoted every other year to this field. In March 2004, NASA Langley Research Center, in conjunction with five other international organizations, held the CFDVAL2004 workshop[1] in Williamsburg, Virginia. The primary objective of this workshop was to assess the state of the art for measuring and computing aerodynamic flows in the presence of synthetic jets. Thomas, Choudhari, and Joslin[2] have conducted an exhaustive and comprehensive survey identifying the feasibility of using active flow control to improve the performance of both external and internal flows. Suggested applications cover a wide range from smart materials and microelectromechanical systems (MEMS) to synthetic (zero net mass flow) jets for enhancing control forces, reducing drag, increasing lift, and enhancing mixing, to name a few. It is also conjectured that active flow control would permit the use of thicker wing sections in non-conventional configurations, such as the blended wing body (BWB) configuration, without compromising the aerodynamic performance.

---

[*]Senior Research Scientist, Senior Member AIAA

[†]Professor, Department of Mathematics, Associate Fellow AIAA

Most of the research in the area of active flow control is of an empirical nature, partially due to the cost and lack of confidence in computational methods for such complex flows. However, without the availability of efficient and well-calibrated computational tools, it will be a very difficult, expensive, and slow process to determine the optimum layout and placement for active flow control devices in practical applications. With the continuous reduction of computer costs in recent years, researchers are devoting more attention to the simulation of such unsteady flows and flow control devices from a computational point of view.[3–8] With few exceptions, most of the numerical studies are undertaken without an active interaction with experimental investigators. Comparisons with experimental data are sometimes done years after the experimental data have been acquired. Under such a scenario, one has to reconstruct many of the details about the experimental arrangement and boundary conditions without the benefit of concrete and consistent information. Based on our experience from previous validation exercises,[9] we recognized the need for active collaboration of the computational and experimental research. Without a symbiotic relationship between the two groups, major misunderstandings can develop when results from these disciplines differ significantly. We were very fortunate to have a cooperative relationship with the researchers conducting the experiments, as well as access to pertinent experimental data.

Our primary objective for this work is to calibrate an existing computational scheme with experimental data for the time-dependent flows encountered in active flow control environments. We devote special attention to establishing appropriate boundary conditions for such flows, especially in the absence of the detailed experimental data required for closure.

The configuration chosen for CFD validation is identified as Case 1 in the CFDVAL2004 workshop[1] and represents an isolated synthetic jet formed by a single diaphragm, piezoelectric actuator exhausting into ambient quiescent air. Multiple measurement techniques, including particle image velocimetry (PIV), laser doppler velocimetry (LDV), and hotwire probes were used to generate a large body of experimental data for this configuration. References 1 and 10 describe the details of the experimental setup and geometric configuration. In this paper, we assess the effects of grid refinement, time-step variation, preconditioning, and turbulence models on the computational simulations of the flow field generated by this flow control device. We model the actuator cavity with a simpler configuration in the present simulations. We demonstrate and calibrate our computational method for simulating synthetic jets by comparing the numerical results with the experimental data.

Governing Equations

A generalized form of the thin layer Navier-Stokes (N-S) equations is used to model the flow. The equation set is obtained from the complete N-S equations by neglecting the cross-derivative terms from the viscous diffusion. Such cross-diffusion terms are significant only in the very small,

$O(\delta \times \delta)$, corner layers and should have negligible effect on the overall accuracy. For a body-fitted coordinate system (ξ, η, ζ) fixed in time, these equations can be written in the conservative form as:

$$Vol\frac{\partial(\mathbf{U})}{\partial t} + \frac{\partial(\mathbf{F} - \mathbf{F_v})}{\partial \xi} + \frac{\partial(\mathbf{G} - \mathbf{G_v})}{\partial \eta} + \frac{\partial(\mathbf{H} - \mathbf{H_v})}{\partial \zeta} = 0 \tag{1}$$

where $\mathbf{U}$ represents the conserved variable vector. The vectors $\mathbf{F}$, $\mathbf{G}$, $\mathbf{H}$, and $\mathbf{F_v}$, $\mathbf{G_v}$, $\mathbf{H_v}$ represent the convective and diffusive fluxes in the three transformed coordinate directions, respectively. In Eq. (1), *Vol* represents the cell volume or the Jacobian of the coordinate transformation. A multigrid-based, multiblock, structured grid, flow solver TLNS3D (thin layer Navier-Stokes three-dimensional), developed at NASA Langley Research Center is used for the solution of the governing equations. References 11 and 12 describe the TLNS3D solver in detail, therefore only a brief summary of its general features is included here.

Discretization

The spatial terms in Eq. (1) are discretized using a cell-centered finite volume scheme. The convection terms are discretized using second-order central differences with a matrix artificial dissipation (second- and fourth-difference dissipation) added to suppress the odd-even decoupling and oscillations in the vicinity of shock waves and stagnation points.[13–15] The viscous terms are discretized with second-order accurate central difference formulas.[11] The zero-equation model of Baldwin-Lomax,[16] one-equation model of Spalart-Allmaras,[17] and Menter's two-equation, shear stress transport (sst) model[18] are available in TLNS3D code for simulating turbulent flows. For the present computations, the Spalart-Allmaras (sa) model and the Menter's (sst) model are used.

Regrouping the terms on the right-hand side into convective and diffusive terms, Eq. (1) can be rewritten as:

$$\frac{d\mathbf{U}}{dt} = -C(\mathbf{U}) + D_p(\mathbf{U}) + D_a(\mathbf{U}) \tag{2}$$

where $C(\mathbf{U})$, $D_p(\mathbf{U})$, and $D_a(\mathbf{U})$ are the convection, physical diffusion, and artificial diffusion terms, respectively. These terms include the cell volume or the Jacobian of the coordinate transformation.

The time-derivative term can be approximated to any desired order of accuracy by a Taylor series

$$\frac{d\mathbf{U}}{dt} = \frac{1}{\Delta t}[a_0\mathbf{U}^{n+1} + a_1\mathbf{U}^n + a_2\mathbf{U}^{n-1} + a_3\mathbf{U}^{n-2} + ...] \tag{3}$$

The superscript n represents the last time level at which the solution is known, and $n+1$ refers to the next time level to which the solution will be advanced. Similarly, $n-1$ refers to the solution

at one time level before the current solution. Eq. (3) represents a generalized backward difference scheme (BDF) in time, where the order of accuracy is determined by the choice of coefficients a_0, a_1, a_2 ... etc. For example, $a_0 = 1.5$, $a_1 = -2$, and $a_2 = .5$ results in a second-order accurate scheme (BDF2) in time, which is the primary scheme chosen for this work because of its unconditional stability and good robustness properties.[19] Regrouping the time-dependent terms and the original steady-state operator leads to the equation:

$$\frac{a_0}{\Delta t}\mathbf{U}^{n+1} + \frac{E(\mathbf{U}^{n,n-1,..})}{\Delta t} = S(\mathbf{U}^n) \tag{4}$$

where $E(\mathbf{U}^{n,n-1,..})$ depends only on the solution vector at time levels n and earlier. S represents the steady-state operator or the right-hand side of Eq. (2). By adding a pseudo-time term, we rewrite the above equation as:

$$\frac{\partial \mathbf{U}}{\partial \tau} + \frac{a_0}{\Delta t}\mathbf{U}^{n+1} + \frac{E(\mathbf{U}^{n,n-1,..})}{\Delta t} = S(\mathbf{U}^n) \tag{5}$$

Solution Algorithm

The algorithm for solving unsteady flow makes extensive use of the steady-state algorithm in the TLNS3D code.[11,12] The basic algorithm consists of a five-stage Runge-Kutta time-stepping scheme for advancing the solution in pseudo-time. Efficiency of this algorithm is enhanced through the use of local time-stepping, residual smoothing, and multigrid techniques developed for solving steady-state equations. Because the Mach number in much of the domain is very low, we consider the use of preconditioning methods[20,21] to improve the efficiency and accuracy of the flow solver.

In order to solve the time-dependent Navier-Stokes equations (Eq. 5), we add another iteration loop in physical time outside the pseudo-time iteration loop. For fixed values of $E(\mathbf{U}^{n,n-1,..})$, we iterate on $\mathbf{U}^{n+1}$ using the standard multigrid procedure of TLNS3D developed for steady-state, until the the pseudo-residual $\frac{a_0}{\Delta t}\mathbf{U} + \frac{E(\mathbf{U})}{\Delta t} - S(\mathbf{U})$ approaches zero. This strategy, originally proposed by Jameson[22] for Euler equations and adapted for the TLNS3D viscous flow solver by Melson et. al,[19] is popularly known as the dual time-stepping scheme for solving unsteady flows. The process is repeated until the desired number of physical time steps is completed. The details of the TLNS3D flow code for solving unsteady flows are available in Ref. 19, 23, 24 and 25.

Boundary Conditions

For the viscous walls, we use the no-slip, no injection, zero pressure gradient and fixed wall temperature conditions for solving the governing equations. For the inviscid walls, we specify zero normal velocity and zero pressure gradient normal to the wall. We apply Riemann invariants based boundary conditions[28] at the far field boundaries.

We apply a periodic velocity transpiration condition at the diaphragm surface to simulate the effect of a moving diaphragm. The frequency of the transpiration velocity in the numerical simulation corresponds to the frequency of the oscillating diaphragm. We determined the peak transpiration velocity from numerical iteration to match the experimentally measured peak velocity at the jet exit. A zero pressure gradient is imposed at this boundary for closure. We also tested the pressure gradient boundary condition obtained from a one-dimensional normal momentum equation.[26] This had very little impact on the solutions. Because of its simplicity and robustness, we selected the zero pressure gradient boundary condition at the diaphragm surface for the present computations.

We set the turbulent eddy viscosity level equal to 1% of the molecular viscosity at the far field and inflow boundaries. At the solid walls, the eddy-viscosity is set equal to zero. Complete details on the boundary condition treatment of turbulence quantities are available in the original papers on these models.[17,18]

Synthetic Jet Test Case: Background

The test configuration examined in this paper is a single diaphragm piezoelectric actuator operating in quiescent air. The oscillatory motion of the diaphragm produces a synthetic jet that exhausts into the surrounding quiescent air. This configuration, shown in Fig. 1(a), consists of a 1.27 mm wide rectangular slot connected to a cavity with a circular piezoelectric diaphragm and corresponds to Case 1 of the CFDVAL2004 workshop on flow control devices.[1] The actuator is connected to a $600 \ mm^3$ enclosure box, such that the slot exit is perfectly matched to a rectangular hole in the base of the enclosure box. Although the cavity and diaphragm geometry of this actuator are highly three-dimensional in the interior, the actual slot through which the fluid emerges is a high aspect ratio rectangular slot and can be modeled as a two-dimensional configuration.

A two-dimensional sectional cut at the midspan location of the physical model depicting the oscillating diaphragm and slot geometry is shown in Fig. 1(b). A multiblock structured grid modeling this simplified geometry was used by the present authors and several of the CFDVAL2004 workshop participants for numerical simulations.[1] The diaphragm motion was simulated via a transpiration condition imposed at the diaphragm surface located at the side of the cavity. Some of the workshop participants further simplified the cavity modeling by imposing a transpiration condition at the bottom part of the slot's neck or even directly at the slot exit. After examining these results, we concluded that as long as the unsteady velocity signal at the slot exit replicates experimental conditions, details of the cavity modeling have an insignificant effect on the development of the synthetic jet emanating from the slot.[1,27]

Results and Discussion

One of the major difficulties identified during the CFDVAL2004 workshop was the large disparity in experimental data obtained from different measurement techniques.[1] Such a variation in experimental data made it difficult to validate the numerical methods. Part of the difficulty in acquiring a consistent set of experimental data arose from the fact that the performance of the piezoelectric diaphragm depends on ambient conditions. Also, its performance degrades over time, which means that, for a given input voltage, the actuator produces smaller jet velocities as it ages. Because these experiments were conducted over several months, inconsistencies crept in the data. Yao et al.[10] have recently revisited the synthetic jet test case and acquired experimental data for this configuration with a new piezoelectric diaphragm. They obtained the detailed field data with the PIV technique and pointwise data along the jet centerline with hotwire and LDV techniques. They monitored the performance of the actuator regularly and demonstrated good consistency among the PIV and LDV measurement techniques.[10] However, the hotwire measurements indicated significant deviation from the PIV and LDV data, especially near solid walls. For this reason, we decided to make use of only the PIV and LDV data for comparison with the computational results in this paper.

Based on the CFDVAL2004 workshop[1] results, it can be concluded that replicating the flow conditions at the slot exit is more important than the detailed modeling of cavity geometry for accurate simulation of the growth of a synthetic jet for this configuration. Therefore, we simulated the new experimental test case with a simplified cavity geometry, shown schematically in Fig. 2(a) and 2(b). We imposed the transpiration condition at the bottom of the slot's neck to simulate the velocity generated by the oscillating diaphragm. A similar boundary condition was used by some of the participants in the CFDVAL2004 workshop.[1] A top-hat velocity profile, with a dominant frequency of 450 Hz replicating the experimental conditions, was imposed at the bottom boundary. The precise temporal variation of the velocity signal was obtained by curve fitting the measured velocities at the slot exit (x = 0, y = 0.3 mm) with a fast Fourier transform (FFT) to reflect the proper mode shape and to ensure zero net mass transfer. The amplitude of this transpiration velocity was determined numerically to match the peak velocity from the experiment at the slot exit. The free stream Mach number in the exterior quiescent region is specified as $M_\infty = .001$ to simulate incompressible flow in the compressible flow code to avoid numerical difficulties at Mach zero. Based on the peak jet velocity and slot width, the Reynolds number is approximately 3000, a regime where the jet is expected to be turbulent. Therefore, we assumed the flow to be fully turbulent in the present computations.

A multiblock structured grid consisting of approximately 61,000 nodes is used as a baseline grid for these computations. This grid is nearly identical to the baseline grid (except for internal cavity region) used by the CFDVAL2004 workshop participants.[1] In addition, a coarse grid (cg)

was created by eliminating every other point in both directions from the baseline grid. Similarly, a finer grid (fg), consisting of approximately 250,000 nodes, was created by doubling the baseline grid in both directions. For efficiency reasons, the finer grid solutions were run on half of the domain by taking advantage of the symmetry along x = 0 plane, and the results were mirrored for plotting purposes about the symmetry plane. Most of the computations were performed using 72 time-steps/period corresponding to a $5°$ phase angle between the time-steps. The effect of temporal resolution was examined by performing computations using 144 time-steps/period. One set of computations was performed with low-speed preconditioning, which had minimal effect on the solutions for this case. Most of the results were obtained with the one-equation Spalart-Allmaras (sa) turbulence model. In addition, the solutions on the baseline grid were also obtained with Menter's (sst) turbulence model.

The TLNS3D code for each case was run long enough to achieve repeatable periodic state for the flow solutions. Starting from the converged solutions, the computations were run for 15 more complete time periods to extract long time-averaged quantities. Taking advantage of the periodic nature of flow, solutions from the last complete time period are used for phase-averaged quantities. Finally, the origin of the phase for experimental and computational results is fixed by shifting the temporal vertical velocity (v-vel) profiles near the slot exit (x = 0, y = 0.3 mm), such that the maximum suction for the experimental and computational velocities occur at the phase of $255°$. This procedure was applied to set the phase for all of the results presented here. Unless mentioned otherwise, the computations were performed on the baseline grid with the Spalart-Allmaras (sa) turbulence model and 72 time-steps/period.

The time history of the phase-averaged v-vel for a complete period from the computational results is compared with the experimental data in Fig. at x = 0 and y = 0.3 mm. This is the closest point to the slot exit where the PIV data is available. LDV measurements are also available at this location and are shown in this figure. The overall agreement between the computational and experimental results is quite good at this location. The four sets of computational results shown in this figure are mostly indistinguishable from one another, indicating a minimal effect of grid density and turbulence model at the slot exit boundary.

In Fig. 4(a), we present the computational results for v-vel along the jet centerline obtained with Spalart-Allmaras (sa) turbulence model for 3 different grids. In addition, we present the results obtained by halving the time-step on the baseline grid. The experimentally measured data from PIV and LDV techniques are also shown in this figure for comparison. The effect of using low speed preconditioning (prec) and Menter's two-equation (sst) model on the baseline grid are shown in Fig. 4(b). The experimental data from two different techniques (PIV and LDV) are in fair agreement with each other. The overall agreement of the baseline TLNS3D results with the experimental data is quite good. In addition, it is observed from Fig. 4(a) that whereas the

effect of refining the grid from coarse (cg) to the baseline grid is significant, further refinement in the grid (fg) has a much smaller effect on these results. Similarly, halving the time-step (i.e. 144 steps/period) from the baseline results (72 steps/period) had insignificant effect on computational results. We note from Fig. 4(b) that the 2-equation turbulence model (sst) results are nearly identical to the baseline (sa) results in the near field (y < 8 mm), but deviate noticeably from the baseline results in regions away from the slot exit (y > 8 mm). On the other hand, the low-speed preconditioning results are essentially identical to the baseline results. Because low-speed preconditioning[20,21,24] primarily reduces the artificial viscosity for unsteady flows, we may infer that the artificial viscosity is low in these simulations, even without preconditioning. The overall numerical accuracy of baseline grid results is considered quite acceptable, considering the uncertainty in physical modeling and turbulence modeling for this problem.

Figures 5 and 6, respectively, show the time-averaged v-vel profiles at y = 1 and 4 mm. Except for a smaller velocity peak at y = 1 mm, the computational results are in very good agreement with the experimental data and with each other at these locations. Only the sst results differ visibly from the rest of the solutions. The effect of the grid refinement is also very small but grows slightly with increasing y values.

Comparing the contour plots of the time-averaged v-vel obtained from measured PIV data and TLNS3D computations (Fig. 7(a) - 7(d)) give a global perspective of the velocity field. Although the computational results are available over a much larger domain, these figures show a domain covering a distance of only 8 mm from the slot exit, corresponding to the region for which the high resolution PIV data was available. The computational results accurately capture all of the prominent features seen in the PIV data, including the width and spreading rate of the synthetic jet. The effect of refining the grid or using Menter's (sst) instead of Spalart-Allmaras (sa) turbulence model over this domain is quite small. The contour plots obtained with preconditioning and smaller time-step (not shown here) are almost identical to the baseline results.

We now examine the phase-averaged velocities at selected locations in space and time, starting with v-vel at y = 2 and 4 mm along the jet center line. Figures 8(a) and 8(b) show the PIV and LDV data, along with TLNS3D solutions at these locations. The computational results are in fairly good agreement with the two sets of experimental data, especially in the suction phase. The agreement with the experimental data further away from the slot exit is slightly worse during the peak expulsion cycle. In particular, the CFD results predict a delayed phase shift for the peak expulsion, reflective of a smaller convective speed for outward movement of the synthetic jet compared to the experimental data. Except for a slightly larger peak velocity for the sst model during the expulsion phase, all four sets of computational results are practically indistinguishable from one another.

We gain a broader perspective of the flow field by examining the contour plots of the veloci-

ties at the phase angles representative of the expulsion (phase = $75°$) and suction (phase = $255°$) cycles. Figures 9-12 show the contour plots for the horizontal and vertical velocities (u-vel and v-vel) obtained from the PIV data and TLNS3D computational results on baseline and finer grid (fg) with the Spalart-Allmaras (sa) turbulence model. Although not shown here, the results obtained with preconditioning and sst turbulence model show very little variation from the baseline solutions. These figures were generated using identical contour levels for both the experimental and CFD data to provide quantitative comparisons. The solid lines represent positive values for the velocities while the dashed lines represent negative values. This sign convention is helpful in identifying the flow direction and the position of the vortex center. It is clear from these figures that the computational results capture most of the pertinent features observed experimentally and are in good agreement for the suction phase (Fig. 11-12). The largest differences are seen in u-vel contours (Fig. 12) in regions away from the slot exit, where the velocities are very small in magnitude. During the expulsion phase (Fig. 9-10), the computed peak velocity at the vortex center is found to be in good agreement with the PIV data, but the computed vortex center is located closer to the slot exit compared to the experimental data. Yao et al.[10] have observed increasing three-dimensional effects for this case as one moves away from the slot exit, mainly because of ring vortices formed from the slot edges. We conjecture that these ring vortices induce forces that accelerate the convection of the synthetic jet in the far field, which can not be simulated by 2-D computations.

Concluding Remarks

Detailed comparisons have been presented for time-averaged and phase-averaged velocities between experimental data and CFD results. The effect of truncation errors were found to be small based on grid refinement, preconditioning, and physical time-step refinement studies. The development of the synthetic jet in the quiescent medium is driven primarily by the velocity field at the slot exit. Hence, formulating this forcing function is much more crucial than detailed modeling of the cavity and parametric variations of the numerical algorithm. The computational results in the reduced domain with a forcing function reflecting the temporal profile at the jet exit are found to be in good agreement with the experimental data in the near field. However, the agreement with the experimental data deteriorates in regions further away from the slot exit. Based on the available experimental data, it appears that the flow becomes three-dimensional after 5-6 slot widths away from the exit. Future work should focus on 3-D computations for this configuration to resolve such issues.

Acknowledgment

imental procedures used for acquiring the data. The authors would also like to acknowledge Dr. Avi Seifert of Tel Aviv University for helpful suggestions regarding boundary condition treatment for synthetic jets, and Dr. C. L. Rumsey of NASA Langley Research Center for helpful discussions on various aspects of this problem.

References

[1] CFD Validation of Synthetic Jets and Turbulent Separation Control: Langley Research Center Workshop, Williamsburg, VA, March 29-31, 2004. (http://cfdval2004.larc.nasa.gov)

[2] Thomas R.H.; Choudhari, M.M.; and Joslin, R.D.: "Flow and Noise Control: Review and Assessment of Future Directions," NASA TM 2002-211631, April 2002.

[3] Hassan, A.A. and Mults, A.A.: "Transverse and Near-Tangent Synthetic Jets for Aerodynamic Flow Control," AIAA Paper 2000-4334, Aug. 2000.

[4] Mittal, R.; Rampunggoon, P.; and Udaykumar, H.S.: "Interaction of a Synthetic Jet with a Flat Plate Boundary Layer," AIAA Paper 2001-2772, June 2001.

[5] Lin, H. and Chieng, C.C.: "Computations of Compressible Synthetic Jet Flows Using Multigrid/Dual Time Stepping Algorithm," AIAA Paper 99-3114, June-July 1999.

[6] Donovan, J.F.; Kral, L.D.; and Cary, A.W.: "Active Flow Control Applied to an Airfoil," AIAA Paper 98-0210, Jan. 1998.

[7] Kral, L.D.; Donoval, J.F.; Cain, A.B.; and Cary, A.W.: "Numerical Simulation of Synthetic Jet Actuators," AIAA Paper 97-1824, June-July 1997.

[8] Joslin, R.D.; Horta, L.G.; and Chen, F.J.: "Transitioning Active Flow Control to Applications," AIAA Paper 99-3575, June-July 1999.

[9] Viken, S.A.; Vatsa, V.N.; Rumsey, C.L.; and Carpenter, M.H.: "Flow Control Analysis on the Hump Model with RANS Tools," AIAA Paper 2003-218, Jan. 2003.

[10] Yao, C.; Chen, F.J.; Neuhart, D.; and Harris, J.: "Synthetic Jet Flow Field Database for CFD Validation," AIAA Paper 2004-2218, June 2004.

[11] Vatsa, V.N. and Wedan, B.W.: "Development of a multigrid code for 3-d Navier-Stokes equations and its application to a grid-refinement study," *Computers and Fluids*, Vol. 18, 1990, pp. 391-403.

[12] Vatsa, V.N.; Sanetrik, M.D.; and Parlette, E.B.: "Development of a Flexible and Efficient Multigrid-Based Multiblock Flow Solver," AIAA Paper 93-0677, Jan. 1993.

[13] Jameson, A.; Schmidt, W.; and Turkel, E.: "Numerical Solutions of the Euler Equations by Finite Volume Methods Using Runge-Kutta Time-Stepping Schemes," AIAA Paper 1981-1259, June 1981.

[14]Turkel, E. and Vatsa, V.N.: "Effect of artificial viscosity on three-dimensional flow solutions," *AIAA Journal*, vol. 32, no. 1, Jan. 1994, pp. 39-45.

[15]Swanson, R.C. and Turkel, E.: "On Central Difference and Upwind Schemes," *Journal of Computational Physics*, vol. 101, 1992, pp. 292-306.

[16]Baldwin,B.S. and Lomax,H.: "Thin layer approximation and algebraic model for separated turbulent flows," AlAA Paper 78-257, Jan. 1978.

[17]Spalart, P.A. and Allmaras, S.R.:"A one-equation turbulence model for aerodynamic flows," AIAA Paper 92-439, Reno, NV, Jan. 1992.

[18]Menter, F.R.: "Zonal Two Equation k-ω Turbulence Models for Aerodynamic Flows," AIAA Paper 93-2906, Orlando, Fl, 1993.

[19]Melson, N.D.; Sanetrik, M.D.; and Atkins, H.L.: "Time-accurate Navier-Stokes calculations with multigrid acceleration," *Proceedings of the Sixth Copper Mountain conference on multigrid methods*, 1993, edited by: Melson, N.D.; Manteuffel, T.A.; and S.F. McCormick, S.F.

[20]Turkel, E.: "Preconditioned Methods for Solving the Incompressible and Low Speed Compressible Equations," *Journal of Computational Physics*, Vol. 72, 1987, pp. 277-298.

[21]Turkel, E.: "Preconditioning Techniques in Computational Fluid Dynamics," *Annual Reviews in Fluid Mechanics*, Vol. 31, 1999, pp. 385-416.

[22]Jameson, A.: "Time Dependent Calculations Using Multigrid, with Applications to Unsteady Flows past Airfoils and Wings," AIAA Paper 91-1596, 1991.

[23]Bijl, H.; Carpenter, M.H.; and Vatsa, V.N.: "Time Integration Schemes for the Unsteady Navier-Stokes Equations," AIAA Paper 2001-2612.

[24]Vatsa, V.N. and Turkel, E.: "Assessment of Local Preconditioners for steady state and time dependent flows," AIAA Paper 2004-2134, June 2004.

[25]Turkel, E. and Vatsa, V.N.: "Local Preconditioners for Steady State and Dual Time-Stepping," *ESAIM: M2AN*, Vol. 39, No. 3, 2005.

[26]Rizzetta, D.P.; Visbal. M.R.; and Stanek, M.J.: "Numerical Investigation of Synthetic Jet Flowfields," AIAA Paper 98-2910, June 1998.

[27]Rumsey, C.L.; Gatski, T.B.; Sellers III, W.L.; Vatsa, V.N.; and Viken, S.A.: "Summary of the 2004 CFD Validation Workshop on Synthetic Jets and Turbulent Separation Control," AIAA Paper 2004-2217, June 2004.

[28]Thomas, J.L. and Salas, M.D.: "Far-Field Boundary Conditions for Transonic Lifting Solutions to the Euler Equations," AIAA Paper 9-85-20, Jan. 1985.
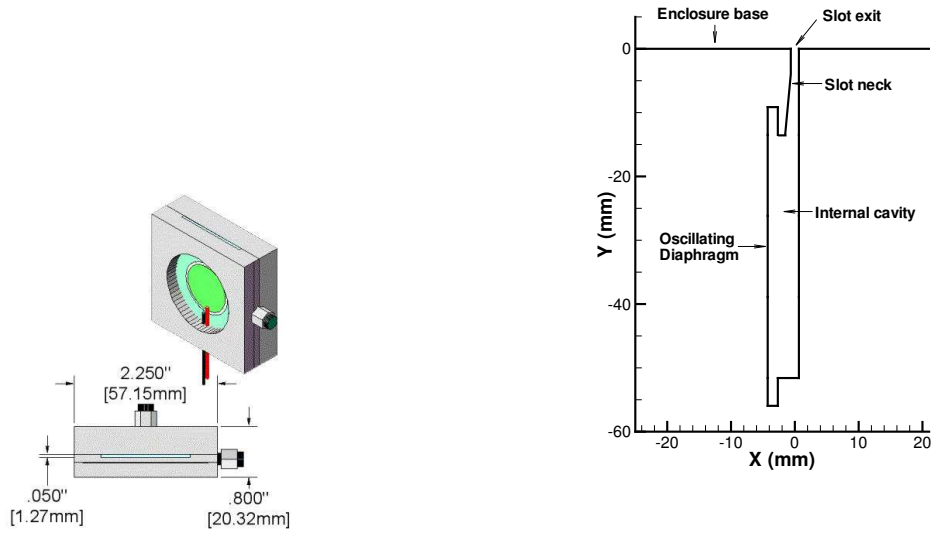
(a) pictorial view of physical model

(b) schematic of 2-D mid-span section

Figure 1 Schematic of piezoelectric actuator
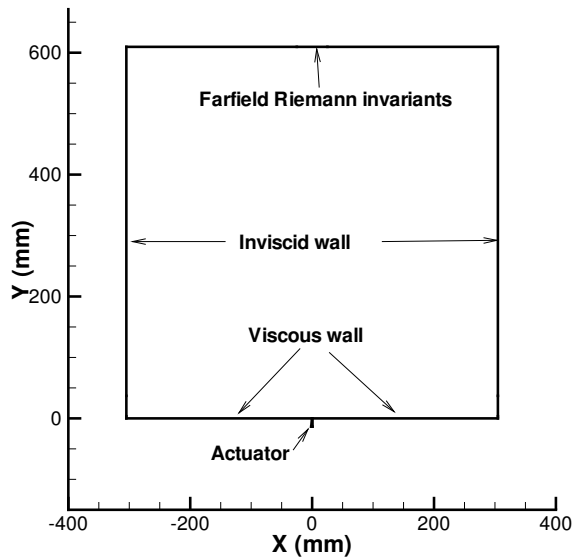
(a) Global view
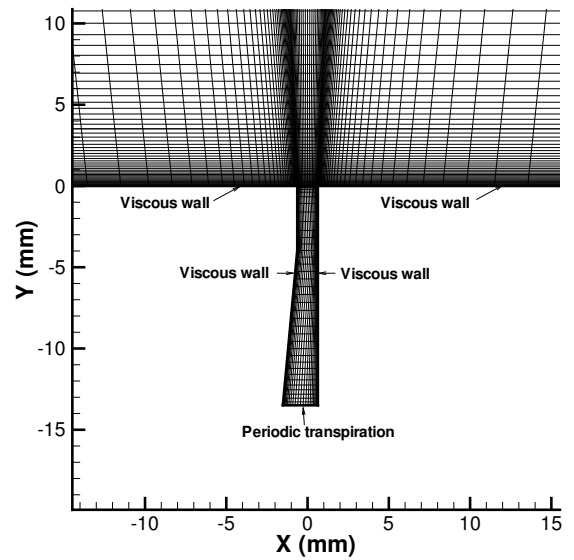
(b) Detailed view

Figure 2 Computational model of piezoelectric actuator
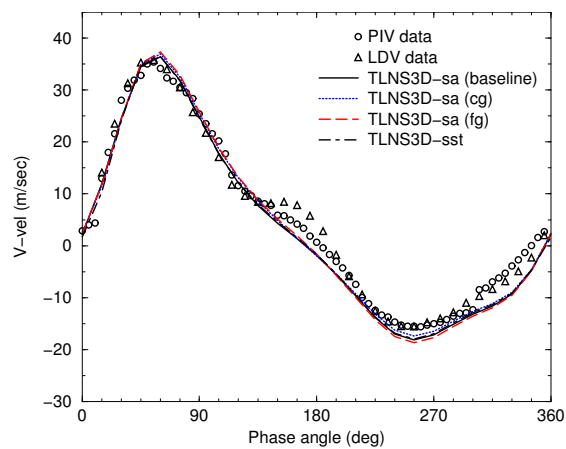
Figure 3 Time history of v-vel near slot exit (x = 0, y = 0.3 mm)
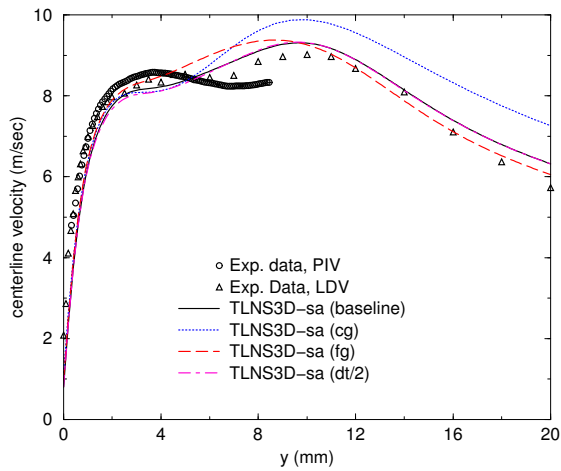
(a) Effect of spatial and truncation errors   (b) Preconditioning and turbulence model effects
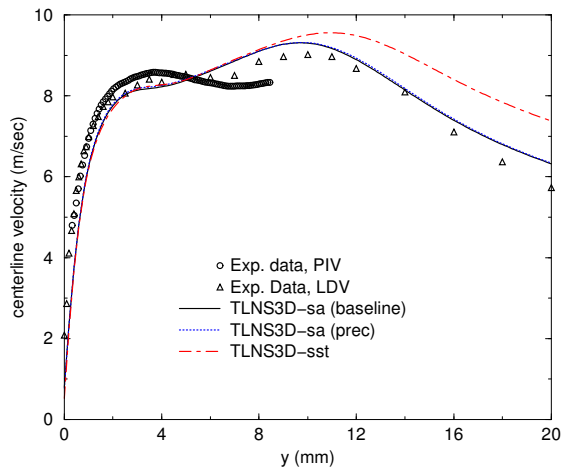
Figure 4 Time-averaged v-vel along centerline
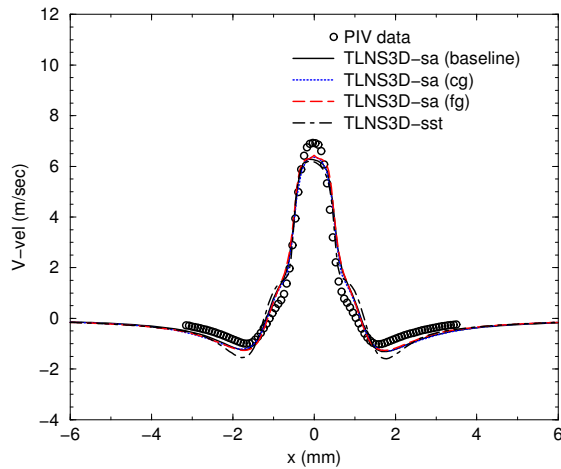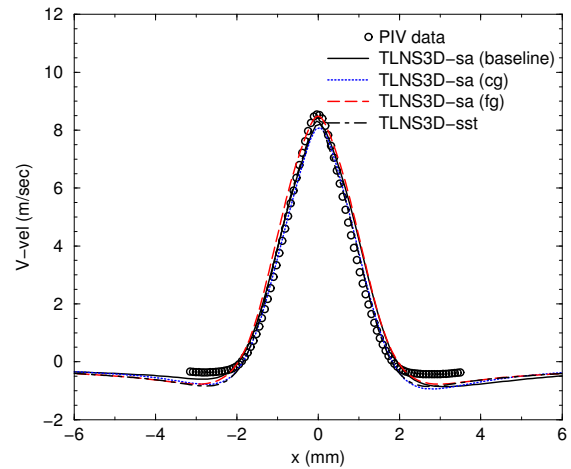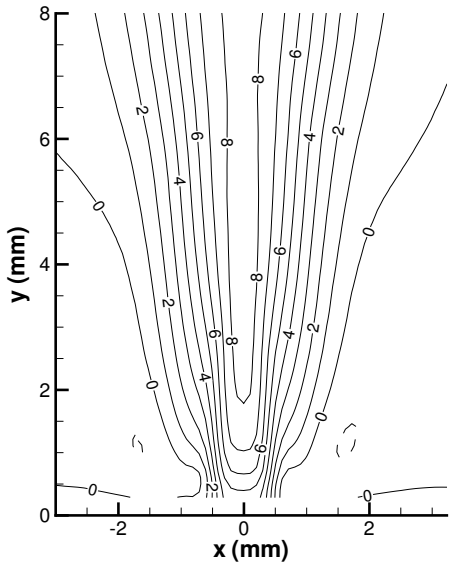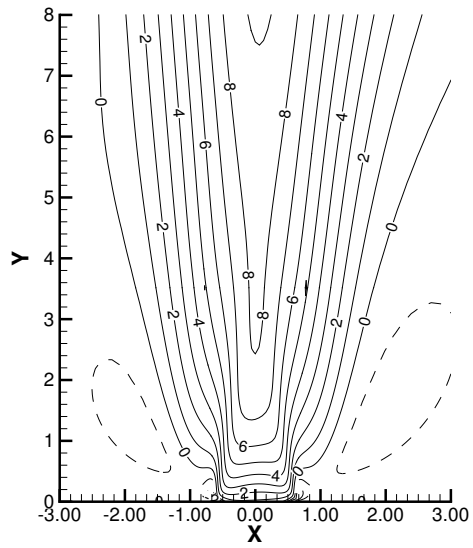

Figure 5 Time-averaged v-vel at y = 1 mm   **Figure 6 Time-averaged v-vel at y = 4 mm**

(a) PIV measurements

(b) TLNS3D-sa (baseline)
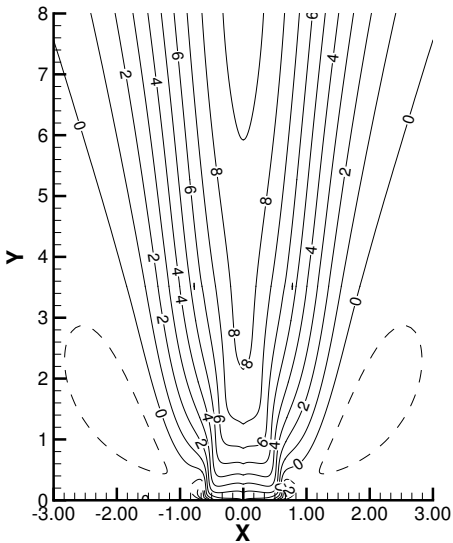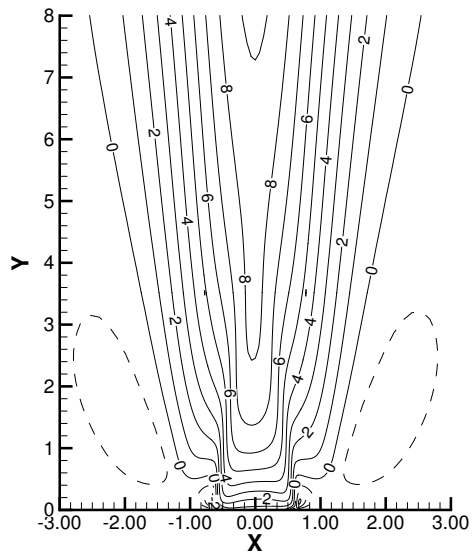
(c) TLNS3D-sa (fg)

(d) TLNS3D-sst (baseline)

Figure 7 Time-averaged v-velocity contour comparisons
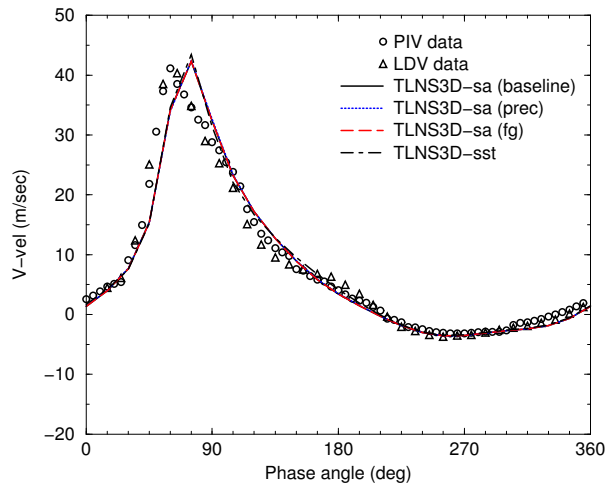
(a) x = 0, y = 2 mm
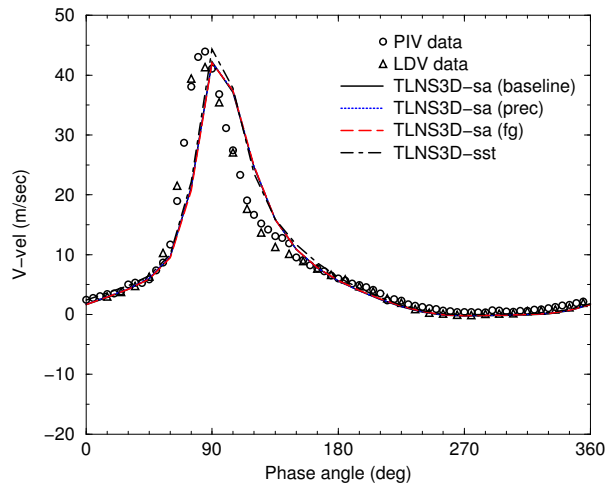
(b) x = 0, y = 4 mm

Figure 8 Phase-averaged v-velocity comparisons
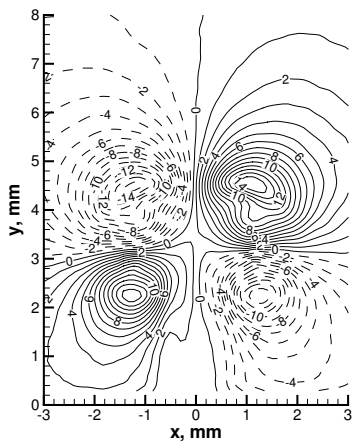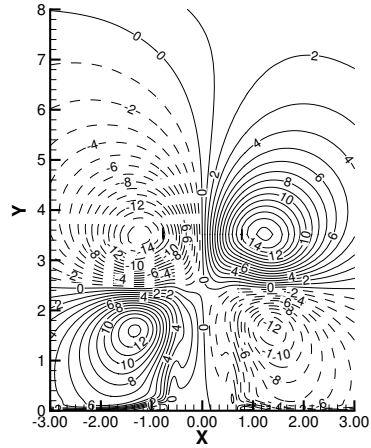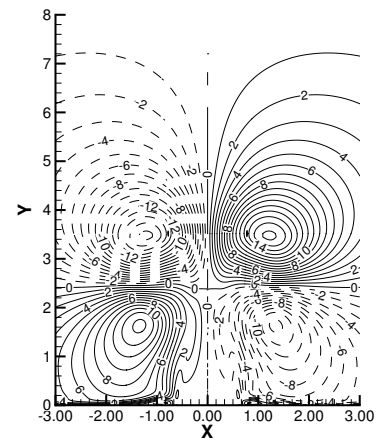
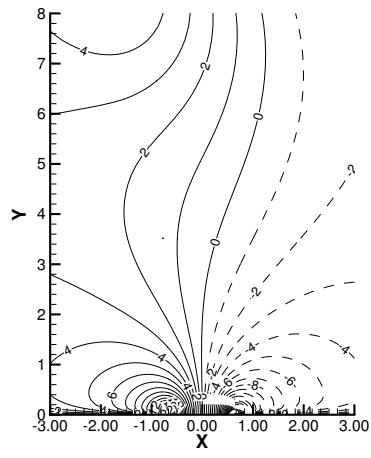(a) PIV measurements   (b) TLNS3D-sa (baseline)   (c) TLNS3D-sa (fg)

Figure 9 Phase-averaged u-velocity contours at expulsion (phase $= 75°$)
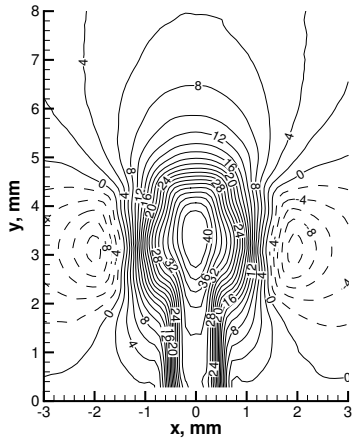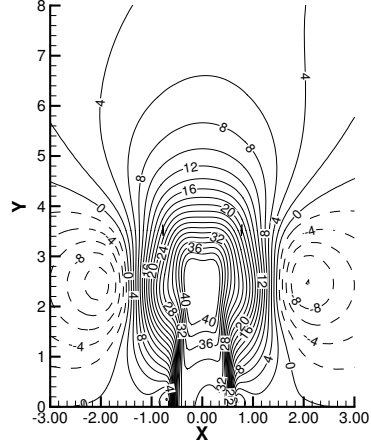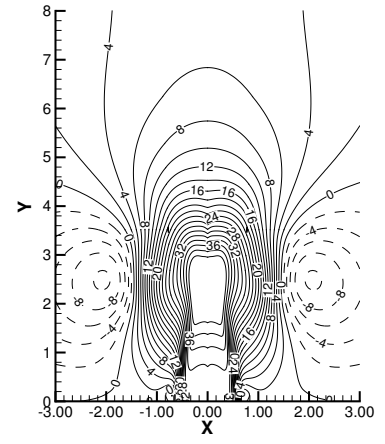
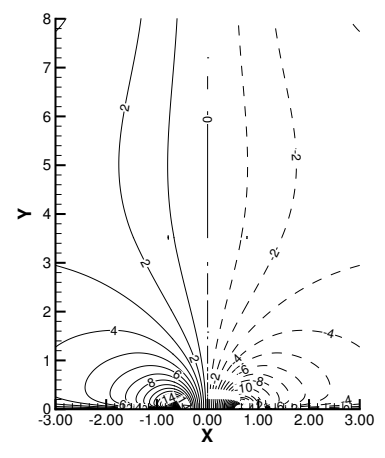(a) PIV measurements   (b) TLNS3D-sa (baseline)   (c) TLNS3D-sa (fg)

Figure 10 Phase-averaged v-velocity contours at expulsion (phase $= 75°$)
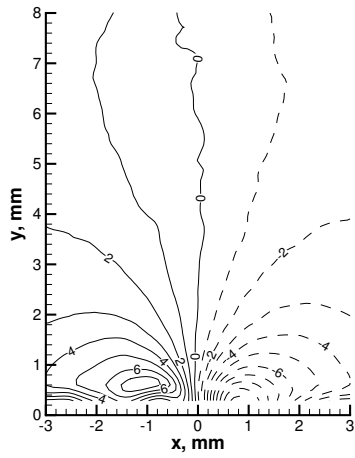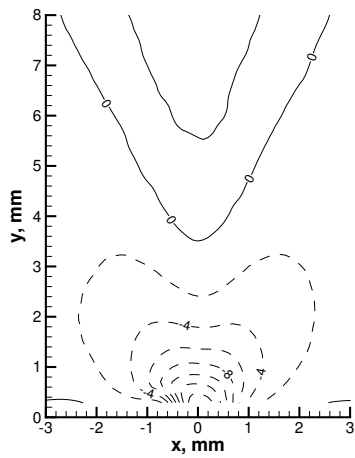
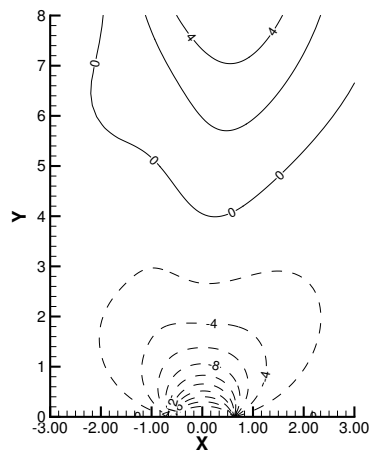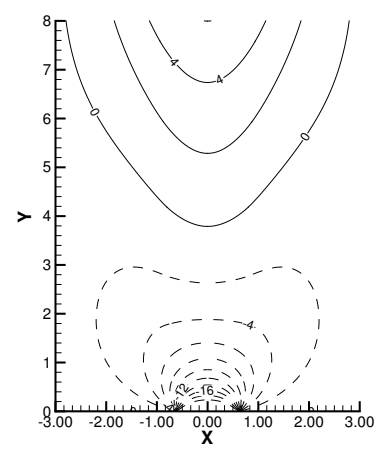(a) PIV measurements   (b) TLNS3D-sa (baseline)   (c) TLNS3D-sa (fg)

Figure 11 Phase-averaged u-velocity contours at suction (phase $= 255°$)

(a) PIV measurements   (b) TLNS3D-sa (baseline)   (c) TLNS3D-sa (fg)

Figure 12 Phase-averaged v-velocity contours at suction (phase $= 255°$)